1 **Influences of an Entrainment-Mixing Parameterization on**

2 **Numerical Simulations of Cumulus and Stratocumulus Clouds**

3   Xiaoqi Xu[1,2,4], Chunsong Lu[1*], Yangang Liu[3*], Shi Luo[1,5], Xin Zhou[3], Satoshi Endo[3],

4   Lei Zhu[1], Yuan Wang[1]

5 1. Key Laboratory for Aerosol-Cloud-Precipitation of China Meteorological

6 Administration/Collaborative Innovation Center on Forecast and Evaluation of

7 Meteorological Disasters (CIC-FEMD), Nanjing University of Information Science &

8 Technology, Nanjing, China

9 2. Nanjing Joint Institute for Atmospheric Sciences, Nanjing, China

10 3. Environmental and Climate Sciences Department, Brookhaven National Laboratory,

11 Upton, US

12 4. Key Laboratory of Transportation Meteorology, CMA, Nanjing, China

13 5. College of Aviation Meteorology, Civil Aviation Flight University of China,

14 Guanghan, China

15 *   Correspondence: luchunsong110@gmail.com; lyg@bnl.gov

Abstract

Different entrainment-mixing processes can occur in clouds; however, a homogeneous mixing mechanism is often implicitly assumed in most commonly used microphysics schemes. Here, we first present a new entrainment-mixing parameterization that uses the grid-mean relative humidity without requiring the relative humidity of the entrained air. Then, the parameterization is implemented in a microphysics scheme in a large eddy simulation model, and sensitivity experiments are conducted to compare the new parameterization with the default homogeneous entrainment-mixing parameterization. The results indicate that the new entrainment-mixing parameterization has a larger impact on the number concentration, volume-mean radius, and cloud optical depth in the stratocumulus case than in the cumulus case. This is because inhomogeneous and homogeneous mixing mechanisms dominate in the stratocumulus and cumulus cases, respectively, which is mainly due to the larger turbulence dissipation rate in the cumulus case. Because stratocumulus clouds break up during the dissipation stage to form cumulus clouds, the effects of this new entrainment-mixing parameterization during the stratocumulus dissipation stage are between those during the stratocumulus mature stage and the cumulus case. A large aerosol concentration can enhance the effects of this new entrainment-mixing parameterization by decreasing the cloud droplet size and evaporation time scale. The results of this new entrainment-mixing parameterization with grid-mean relative humidity are validated by use of a different entrainment-mixing parameterization that uses parameterized

38 entrained air properties. This study sheds new light on the improvement of entrainment-

39 mixing parameterizations in models.

1. Introduction

42   The process of entrainment and subsequent mixing between clouds and their

43 environment is one of the most uncertain processes in cloud physics, which is thought

44 to be crucial to many outstanding issues, including warm-rain initiation and subsequent

45 precipitation characteristics, cloud-climate feedback, and evaluating the indirect effects

46 of aerosol (Paluch and Baumgardner, 1989; Yum, 1998; Ackerman et al., 2004; Kim et

47 al., 2008; Huang et al., 2008; Del Genio and Wu, 2010; Lu et al., 2011; Lu et al., 2014;

48 Kumar et al., 2013; Zheng and Rosenfeld, 2015; Fan et al., 2016; Gao et al., 2020; Gao

49 et al., 2021; Zhu et al., 2021; Xu et al., 2021; Kumar et al., 2013; Yang et al., 2016;

50 Yang et al., 2021). The most well-studied concepts are homogeneous/inhomogeneous

51 entrainment-mixing mechanisms. During homogeneous mixing, all droplets experience

52 evaporation, and no droplet is evaporated completely. During extremely

53 inhomogeneous mixing, some droplets near the entrained air evaporate completely,

54 while the remaining droplets maintain their original sizes. If the situation is somewhere

55 between these two extreme scenarios, an inhomogeneous mixing process occurs. Some

56 studies suggest that homogeneous mixing is likely to be typical (Jensen et al., 1985;

57 Burnet and Brenguier, 2007; Lehmann et al., 2009), whereas others have claimed that

58 extremely inhomogeneous scenario is dominant (Pawlowska et al., 2000; Burnet and

59 Brenguier, 2007; Haman et al., 2007; Freud et al., 2008; Freud et al., 2011). Different

60 mechanisms can be undistinguishable when the relative humidity in the entrained air is

61 high (Gerber et al., 2008).

62   Some sensitivity studies assuming homogeneous or extremely inhomogeneous

63 mixing have found that different mixing mechanisms can significantly influence the

64 microphysics and radiative properties of clouds (Lasher-Trapp et al., 2005; Grabowski,

65 2006; Chosson et al., 2007; Slawinska et al., 2008). For example, Grabowski (2006)

66 used a cloud-resolving model and found that the amount of solar energy reaching the

67 surface in the pristine case, assuming the homogeneous mixing scenario, is the same as

68 in the polluted case with extremely inhomogeneous mixing. This result was verified by

69 Slawinska et al. (2008) using a large-eddy simulation (LES) model. Although the

70 influence of different mixing mechanisms in simulations is lower when two-moment

71 microphysics schemes are used (Hill et al., 2009; Grabowski and Morrison, 2011;

72 Slawinska et al., 2012; Xu et al., 2020), Hill et al. (2009) also claimed that there are

73 still many uncertainties in the entrainment-mixing process, and the effect of different

74 mixing mechanisms can be more important over the entire cloud life-cycle.

75   In recent years, methods have been developed to describe general entrainment-

76 mixing processes, with homogeneous and extremely inhomogeneous scenarios as

77 special cases (Andrejczuk et al., 2006; Andrejczuk et al., 2009; Lehmann et al., 2009;

78 Lu et al., 2011). Hoffmann et al. (2019) and Hoffmann and Feingold (2019) conducted

79 LES at the subgrid-scale with turbulent mixing, using a linear eddy model. Andrejczuk

80   et al. (2009) used the results of direct numerical simulation (DNS) to establish a

81   relationship between instantaneous microphysical properties and Damköhler number

82   (D_a, Burnet and Brenguier, 2007), and developed a parameterization of the entrainment-

83   mixing process. Lu et al. (2013) developed a parameterization of the entrainment-

84   mixing process based on the relationship between the homogeneous mixing degree (ψ)

85   and transition scale number (N_L) in the explicit mixing parcel model (EMPM), as well

86   as aircraft observation data. Gao et al. (2018) investigated how ψ is related to D_a and

87   N_L in a DNS, to improve the parameterization of the entrainment-mixing process. Luo

88   et al. (2020) simulated more than 12,000 cases with EMPM by changing a variety of

89   parameters affecting entrainment-mixing processes and developed a parameterization

90   that improved the one proposed by Lu et al. (2013).

91   Although several entrainment-mixing parametrizations have been proposed, to the

92   best of our knowledge, only one study (Jarecka et al., 2013) has coupled an entrainment-

93   mixing parameterization with cloud microphysics to consider the change in cloud

94   droplet concentration during the entrainment-mixing process. Jarecka et al. (2013)

95   applied an entrainment-mixing parameterization, in terms of the Damköhler number, to

96   a two-moment microphysics scheme and found small impacts of entrainment-mixing

97   parameterization in shallow cumulus clouds. To further explore the influences of

98   entrainment-mixing processes, this study first modifies the entrainment-mixing

99   parameterization in terms of the transition scale number proposed by Luo et al. (2020)

100   to couple it more easily with microphysics schemes. The parameterization is then

101 implemented in the two-moment Thompson aerosol-aware scheme (Thompson and

102 Eidhammer, 2014). Finally, the effects of parameterization on the physical properties

103 of clouds are examined in both cumulus and stratocumulus clouds.

104   The rest of this paper is organized as follows: Section 2 describes the new

105 entrainment-mixing parameterization, simulated cases, and modelling setup. The major

106 results are presented and discussed in Section 3. The influences of the new entrainment-

107 mixing parameterization on cloud physics and the underlying mechanisms are

108 examined, and the effects of turbulence dissipation rate (ε) and aerosol concentration

109 are also discussed. Some concluding remarks are presented in Section 4.

110

111 **2. Parameterization, simulated cases, and modeling setup**

112 **2.1 The new entrainment-mixing parameterization**

113   According to Morrison and Grabowski (2008), the effect of the entrainment-

114 mixing process on cloud microphysical properties can be expressed as follows:

115
$$N_c = N_{c0}\left(\frac{q_c}{q_{c0}}\right)^{\alpha},$$
(1)

116 where N_c and N_{c0} are the cloud droplet number concentrations after and before the

117 evaporation process, respectively, and q_c and q_{c0} represent the corresponding cloud

118 water mixing ratios. It is noteworthy that when a new saturation is achieved after

119 evaporation, q_c is determined by q_{c0}, relative humidity (RH), air pressure, and

120 temperature. The parameter α can be pre-set to any value between 0 (homogeneous

121 mixing) and 1 (extremely inhomogeneous mixing) to represent a different degree of

122   subgrid-scale mixing homogeneity. In this study, instead of specifying α as a

123   predetermined constant, here it is determined through expressions (Lu et al., 2013; Luo

124   et al., 2020)

$$\alpha = 1 - \psi, \tag{2a}$$

$$\psi = c \exp(a N_{\mathrm{L}}^{b}). \tag{2b}$$

127   where a, b and c are the three fitting parameters (Luo et al., 2020). The dimensionless

128   number N_{L} is a dynamical measure of the degree of subgrid-scale mixing homogeneity

129   (Lu et al., 2011) defined by

$$N_{\mathrm{L}} = \frac{L^{*}}{\eta}, \tag{3a}$$

$$\eta = \left(v^{3} / \varepsilon \right)^{1/4}, \tag{3b}$$

$$L^{*} = \varepsilon^{1/2} \tau_{\mathrm{evap}}^{3/2}, \tag{3c}$$

133   where L^{*} is the transition length (Lehmann et al., 2009), η is the Kolmogorov microscale,

134   v is the kinematic viscosity; ε is calculated from the subgrid turbulent kinetic energy

135   (Deardorff, 1980):

$$\varepsilon = C E^{3/2} / L, \tag{4}$$

137   where $C = 0.70$ is an empirical constant, E is the subgrid turbulent kinetic energy, and

138   L is the model grid size. The evaporation time scale (τ_{evap}) is defined as the time taken

139   for droplets to evaporate completely in an unsaturated environment, and is calculated

140   as

$$\tau_{\mathrm{evap}} = -\frac{r^{2}}{2 A S_{\mathrm{e}}}, \tag{5a}$$

142
$$A = \frac{1}{\left[\left(\dfrac{L_h}{R_v T} - 1\right)\dfrac{L_h \rho_L}{KT} + \dfrac{\rho_L R_v T}{D e_s(T)}\right]},$$ (5b)

143 where r is the volume-mean radius of cloud droplets, A is a function of pressure and

144 temperature, S_e is the supersaturation (RH-1) of entrained air, L_h is the latent heat, R_v is

145 the specific gas constant for water vapour, T is air temperature, ρ_L is the density of liquid

146 water, K is the coefficient of thermal conductivity of air, D is the diffusion coefficient

147 of water vapour in the air, and $e_s(T)$ is the saturation vapour pressure over a plane water

148 surface at temperature T.

149   Unfortunately, S_e in Equation (5a) is generally unavailable in atmospheric models,

150 including LES models. Thus, the entrainment-mixing parameterization developed by

151 Luo et al. (2020) based on the properties of entrained air cannot be used directly. To

152 solve this problem, we modify the entrainment-mixing parameterization of Luo et al.

153 (2020) by replacing S_e with the domain-mean RH in the EMPM, after entrainment but

154 before evaporation, based on 12,218 cases:

155
$$\psi = 107.19 \exp(-1.99 N_L^{-0.29}).$$ (6)

156 Figure 1 shows the fitting results of the modified new entrainment-mixing

157 parameterization. Compared to the parametrization proposed by Luo et al. (2020), the

158 modified parameterization has similar ψ-N_L distributions, but with a larger N_L for the

159 same ψ, because the EMPM domain-mean RH is larger than the entrained air RH. With

160 this modification, N_L, ψ, and thus the effect of the entrainment-mixing processes on

161 droplet concentration can be directly calculated using the LES grid-mean RH. It is

162   important to note that the parameterization does not mean that the entrained air RH is

163   equal to that of the LES grid-mean RH. It is also worth noting that a wide range of ε,

164   S_e, and fraction of entrained air (f) are taken into account when establishing the

165   parameterization with the EMPM. The details of the EMPM simulations and related

166   calculations are provided by Luo et al. (2020).

167

168   **2.2 LES model, simulation cases, and modelling setup**

169   The LES model is built by applying the large-scale forcing module presented in

170   Endo et al. (2015) to the Weather Research and Forecasting (WRF) model tailored for

171   solar irradiance forecasting (WRF-Solar, Hacker et al., 2016; Haupt et al., 2016). The

172   large-scale forcing data (VARANAL) used in this process is derived from the

173   constrained variational analysis (CVA) approach developed by Zhang et al. (2001) and

174   provided by the U.S. Department of Energy's Atmospheric Radiation Measurement

175   Program (www.arm.gov). The modified entrainment-mixing parameterization is

176   implemented in the two-moment Thompson aerosol-aware scheme (Thompson and

177   Eidhammer, 2014).

178   To investigate the behaviours of the new entrainment-mixing parameterization in

179   different cloud types, cumulus and stratocumulus cases are simulated. For both the

180   cumulus and stratocumulus cases, the horizontal resolution of the model is 100 m × 100

181   m with a domain area of 14.4 km × 14.4 km. The vertical direction is divided into 225

182   layers with a resolution of 30 m.

183   For each cloud case, ψ is first set to 1 for the *default* experiment because most LES

184   models assume a homogeneous entrainment-mixing mechanism. The simulation with

185   the new entrainment-mixing parameterization (Equations (1-6)) is hereafter referred to

186   as *new*. First, N_L is diagnosed for each grid, and ψ is then calculated using Equation (6).

187   Finally, the variation in N_c during entrainment-mixing is obtained using Equations (1)

188   and (2a). To examine the influence of the aerosol number concentration on the

189   entrainment-mixing process, we conduct the numerical experiments *default_10* and

190   *new_10* by multiplying the initial aerosol number concentrations, for the *default* and

191   *new* models, respectively, by a factor of 10. Thus, four sets of numerical experiments

192   are conducted for both the cumulus and stratocumulus cases; the names of the

193   experiments and corresponding descriptions are summarized in Table 1.

194

195   **3. Results**

196   **3.1 Cumulus case**

197   For the cumulus case, the simulation starts at 12:00 UTC on 11 June 2016 and

198   ends at 03:00 UTC on 12 June 2016 with an output interval of 10 min and spin-times

199   of 3 h. To demonstrate the utility of the model, Figure 2 compares the temporal

200   evolution of the observed and simulated cloud fraction (a) and solar irradiance (b) from

201   the *default* experiment. Grid points with q_c larger than 0.01 g/kg are defined as "cloudy

202   areas". Also shown for comparison is observational data with a one-hour temporal

203   resolution, which is provided by the LES Atmospheric Radiation Measurement

204   Symbiotic Simulation and Observation (LASSO) campaign (Gustafson et al., 2020).

205   The observations show that the cloud forms at 12:00 UTC on 11 June and dissipates

206   completely by 01:00 UTC on 12 June with a maximum cloud fraction of 0.47 at 16:00

207   UTC on 11 June. Considering the difference between the solar irradiances obtained

208   from point measurements and the value representing the simulation domain, the

209   observed solar irradiance at the Southern Great Plains (SGP) Central Facility are

210   compared with the results of central grid point in simulation (Figure 2(b)). Evidently,

211   although the results of simulation do not fluctuate as much as the observations, the

212   model captures the general behaviours of both cloud fraction and solar irradiance. The

213   general agreement between the simulations and observations lends credence to using

214   the model in further study.

215   Figure 3 shows the evolution of the microphysical and optical properties of clouds

216   in the cloudy areas of all simulation experiments, including q_c, N_c, droplet volume-

217   mean radius (r_v), cloud water path (CWP), and cloud optical depth (τ). To visually and

218   simultaneously compare the change in cloud droplet concentration under different

219   aerosol concentrations, the maximum cloud droplet concentration (N_{cmax}) from *default*

220   is used to normalize N_c in *default* and *new*, while N_{cmax} from *new_10* is used to

221   normalize N_c in *default_10* and *new_10*. The CWP is calculated as:

222 $$\text{CWP} = \int_0^H \rho_a q_c(z) dz, \tag{7}$$

223   where ρ_a is the air density, $q_c(z)$ is the cloud water mixing ratio at each height (z), and

224   *H* is the cloud thickness. The optical depth τ is estimated with

225
$$\tau = \frac{3}{2}\frac{1}{\rho_{\mathrm{w}}}\int_{0}^{H}\frac{\rho_{\mathrm{a}}q_{\mathrm{c}}(z)}{r_{\mathrm{e}}(z)}\,dz, \tag{8}$$

226 where ρ_{w} is the water density and $r_{\mathrm{e}}(z)$ is the effective radius of the cloud droplets at

227 each height (z). The time-averaged values of these physical properties of the clouds are

228 listed in Table 2 for convenience.

229   For the low aerosol number concentration, the simulations with the new

230 entrainment-mixing parameterization have smaller N_{c} (35.53 cm^{-3}) and larger r_{v} (13.29

231 μm) than the default homogeneous simulation (35.78 cm^{-3} for N_{c} and 13.27 μm for r_{v}

232 in *default*). However, comparing *new* to *default*, the relative changes in N_{c}, r_{v}, and τ are

233 very small. When the aerosol concentration increases ten-fold (*default_10* and *new_10*),

234 q_{c}, CWP, and τ increase according to the aerosol indirect effect (Peng et al., 2002; Wang

235 et al., 2019; Li et al., 2011; Wang et al., 2011). Meanwhile, r_{v} decreases significantly

236 owing to the larger cloud number concentration. The effects of the new entrainment-

237 mixing parameterization also increase, for example, the change in N_{c} increases from –

238 0.70% (*new* compared to *default*) to –2.74% (*new_10* compared to *default_10*), r_{v}

239 increases from +0.15% to +0.57%, and τ from –0.38% to –0.58%; the reasons for these

240 changes are discussed later. These small changes are similar to those identified in

241 previous cumulus studies (Jarecka et al., 2013; Hoffmann et al., 2019).

242

243 **3.2 Stratocumulus case**

244   The stratocumulus case is simulated from 9:00 UTC on 19 April 2009 to 03:00

245 UTC on 20 April 2009; the first three hours are set to be spin-up times. We examine the

246   stratocumulus region of the cloud base at ~2.1 km and the cloud top at ~2.3 km (cloud

247   thickness of ~200 m). Figure 4 shows the time series of the domain-averaged cloud

248   fraction and total downward irradiance at the central point in the observation and the

249   *default* experiment from 12:00 UTC to 24:00 UTC. Similar to the cumulus case, the

250   simulations compare favourably with the observations, which further reinforces the

251   utility of the LES model. The observed data show that the cloud fraction increases with

252   time and peaks at 16:00 UTC. The simulated cloud fraction has a value of 1 before

253   16:00 UTC, fluctuates from 16:00 UTC to 21:00 UTC, and decreases sharply after

254   21:00 UTC. This period can be divided into three stages, namely the mature stage, pre-

255   dissipation stage, and dissipation stage.

256   As with the cumulus case, the temporal evolutions of the physical properties (q_c,

257   N_c, r_v, CWP, and τ) of the clouds are shown in Figure 5. In contrast to the oscillating

258   changes exhibited by the physical quantities in the cumulus case (Figure 3), the physical

259   properties in the stratocumulus case exhibit a mostly smooth temporal evolution.

260   Furthermore, *default* and *new* exhibit clear distinctions during the early periods, but

261   these differences decrease during the dissipation stage. This is also the case with

262   *default_10* and *new_10*.

263   To compare the different behaviours of the simulation experiments at different

264   stages, the results at the mature and dissipation stages are analysed in detail. The mean

265   values of the main microphysical and optical properties of the clouds are summarised

266   in Table 3. As expected, the cloud microphysical and optical properties at the mature

267   stage are all larger than those at the dissipation stage. The effects of the new

268   entrainment-mixing parametrization are also more significant at the mature stage.

269   Compared to *default*, the *new* model results in a 7.36% smaller N_c, 3.20% larger r_v, and

270   5.98% smaller τ during the mature stage. During the dissipation stage, the changes in

271   N_c, r_v, and τ are –4.76%, +2.12 %, and –2.56%, respectively. The largest influence of

272   the new entrainment-mixing parametrization occurs during the mature stage when the

273   aerosol concentration is ten times greater. The differences in N_c, r_v, and τ between

274   *new_10* and *default_10* are –9.69%, +3.88%, and –5.85%, respectively, averaged over

275   the mature stage. These differences are much larger than those reported by Hill et al.

276   (2009) who found that assuming extremely inhomogeneous mixing has a negligible

277   effect on stratocumulus simulations. Our results also prove the speculation of Hill et al.

278   (2009) that the mixing process might play an important role when the stratocumulus is

279   thin (~200 m in this study). Furthermore, implementing the new entrainment-mixing

280   parameterization has similar effects on cloud properties to those described by Hoffmann

281   and Feingold (2019) who used the linear eddy model to represent subgrid-scale

282   turbulent mixing. Note that stratocumulus clouds occur in most regions around the

283   world and are important contributors to the surface radiation budget (Wood, 2012;

284   Zheng et al., 2016; Wang et al., 2021; Wang and Feingold, 2009). Stratocumulus clouds

285   dominate in some regions and occur over 60% of the time as vast long-lived sheets,

286   such as the *semi-permanent subtropical marine stratocumulus sheets* (Wood, 2012). In

287   these regions, a nearly 6% decrease in τ, caused by the new entrainment-mixing

288 parameterization is expected to have significant effects on the simulation of regional

289 radiative properties and climate change.

290   The averaged influences of the new entrainment-mixing parametrization over all

291 the simulation periods are also examined (Table 4). Quantitatively, the effect of the new

292 entrainment-mixing parameterization is much greater on stratocumulus clouds than on

293 cumulus clouds. Compared to *default*, *new* has an average change of –6.20% in N_c,

294 +2.01% in r_v, and –3.23% in τ. When the aerosol concentration increases ten-fold, the

295 differences in N_c, r_v, and τ between *default_10* and *new_10* are −9.00%, +3.16%, and

296 −4.14%, respectively. These differences are larger than the largest changes in the

297 cumulus case.

298

299 **3.3 Mechanisms of the effects of the new entrainment-mixing parameterization**

300   The different effects of the new entrainment-mixing parameterization on different

301 types of clouds and even on different stages of stratocumulus clouds are likely be related

302 to variations in the dominant mixing mechanism. To confirm this, we calculate the

303 average ψ at all grid points experiencing evaporation, the proportion of inhomogeneous

304 mixing grid points to all grid points experiencing evaporation, and the average ψ at the

305 inhomogeneous mixing grid points in *new* and *new_10* (Table 5) for the cumulus case,

306 and mature and dissipation stages in the stratocumulus case.

307   For the cumulus case, simulations exhibit large ψ and a small proportion of

308 inhomogeneous mixing, indicating that homogeneous mixing is the dominant

309 entrainment-mixing mechanism (Luo et al., 2020; Lu et al., 2013). Correspondingly,

310 the influences of the new entrainment-mixing parameterization on the cloud physical

311 properties are not significant, as shown in Figure 3 and Table 2. The *new_10* model

312 exhibit a smaller average ψ and a larger proportion of inhomogeneous mixing than *new*,

313 which results in larger changes in cloud physics, as mentioned in Section 3.1.

314   For the stratocumulus case, Table 5 shows the average ψ at all grid points

315 experiencing evaporation, the proportion of inhomogeneous mixing grid points to all

316 grid points experiencing evaporation, and the average ψ at the inhomogeneous mixing

317 grid points during the two stages. The mature stage always has a smaller ψ but a larger

318 proportion of inhomogeneous mixing than the dissipation stage. The inhomogeneous

319 mixing process dominates the mature stage in *new*, because more than 60% of the grid

320 points experience inhomogeneous mixing. The inhomogeneous mixing process is more

321 dominant in *new_10*, because less than 3% of the cloudy grid points experience a

322 homogeneous mixing process during the mature stage, which explains why *new_10* has

323 the largest influence when implementing the new entrainment-mixing parametrization.

324 Meanwhile, the average ψ in both stages is smaller than that in the cumulus case for the

325 same simulation configuration. Thus, the effects of the new entrainment-mixing

326 parameterization are more significant for stratocumulus than for cumulus clouds,

327 especially at the mature stage. It is noted that the average ψ and the proportion of

328 inhomogeneous mixing at the dissipation stage of *new* in the stratocumulus case are

329 very close to the results of *new_10* in the cumulus case. This is because the cloud

330   fraction decreases sharply during the dissipation stage; the stratocumulus clouds break

331   up and produces cumulus clouds with small cloud droplet radius.

332

333   **3.4 The effects of dissipation rate and aerosol concentration on the entrainment-**

334   **mixing process**

335   Previous studies have shown the notable effects of the dissipation rate and aerosol

336   concentration on the entrainment-mixing process. For example, Luo et al. (2020)

337   changed ε from 10^{-5} m^2 s^{-3} to 10^{-2} m^2 s^{-3} and noted huge differences in the corresponding

338   ψ. Small et al. (2013) compared aircraft observations with different background

339   concentrations and found that higher pollution flights tended to slightly more

340   inhomogeneous mixing; Jarecka et al. (2013) also showed various homogeneities of

341   subgrid mixing when aerosol concentration increases ten-fold. To explain the different

342   behaviours of different simulations with the new entrainment-mixing parameterization,

343   the influences of ε and aerosol concentration are examined. Figure 6 shows the

344   probability distribution functions (PDFs) of ε, r_v, τ_{evap}, and N_L for cloud grids

345   experiencing entrainment-mixing processes in *new* and *new_10* for the cumulus and

346   stratocumulus cases, respectively. The PDFs from the mature and dissipation stages of

347   the stratocumulus case are shown in Figure 7.

348

349   **3.4.1 Dissipation rate**

350   According to Equation (3), N_L is a function of $\varepsilon^{3/4}$; hence, the PDF of ε directly

351   affects N_L and further results in different ψ. For the cumulus case, the mean ε of 0.0043

352   m^2 s^{-3} in *new* is similar to those obtained for cumulus clouds in previous studies (e.g.

353   Lu et al., 2016; Hoffmann et al., 2019). As shown in Figure 1, cloud grids experience a

354   homogeneous mixing process if N_L is larger than $\sim 10^5$, the limited distribution of N_L

355   values less than 10^5 in *new* results in a very small number of cloud grid points

356   undergoing inhomogeneous mixing process. Even at the cloud grid points that undergo

357   inhomogeneous mixing, the average ψ is large (98.62%), because most of the N_L values

358   are larger than 10^3. Therefore, the cloud properties in *new* are close to those in *default*.

359   For the stratocumulus case, the mean value of ε (2.9×10^{-4} m^2 s^{-3} in *new*) is an order

360   of magnitude less than those in the cumulus case. Therefore, compared with the

361   cumulus case, N_L is reduced in the stratocumulus case, while the peak value of *new*

362   almost reaches the criterion of inhomogeneous mixing ($\sim 10^5$). For the two stages of

363   stratocumulus clouds, ε is an order of magnitude smaller, but r_v was larger (Figure 7)

364   during the mature stage than during the dissipation stage. According to Equation (5a),

365   droplets with smaller r_v are more prone to complete evaporation and have a smaller τ_{evap}.

366   The combination of smaller ε and larger r_v results in a smaller N_L (Equation (3)). This

367   is the reason for the new entrainment-mixing parametrization having more significant

368   effects during the mature stage than during the dissipation stage. In addition, the

369   similarity of the ε and r_v values during the dissipation stage of the stratocumulus case

370   in *new*, compared to the cumulus case in *new_10* (Figures 6a and 6b), explains the

371   similar average ψ values of these scenarios and the proportion of inhomogeneous

372   mixing (Table 5).

373   Therefore, the distribution of ε has a vital impact on the influence of the new

374   entrainment-mixing parameterization. Smaller values of ε result in the new

375   entrainment-mixing parameterization having a more significant influence. Moreover,

376   the r_v in the stratocumulus case is smaller than that in the cumulus case, which is also

377   conducive to a more inhomogeneous mixing process. These are the reasons why the

378   implementation of the new entrainment-mixing parameterization has a larger influence

379   in the stratocumulus case than in the cumulus case, when compared to a homogeneous

380   mixing mechanism.

381

382   **3.4.2 Aerosol concentration**

383   The aerosol concentration affects the entrainment-mixing process by decreasing

384   the cloud droplet radius. As r_v decreases, the distributions of τ_{evap} in *new_10* moves to

385   a smaller overall value, while the mean value is an order of magnitude smaller than that

386   in *new*, which causes a much smaller N_L because N_L is proportional to $\tau_{\text{evap}}^{3/2}$ (Equations

387   (3a) and (3b)). The larger percentage of smaller N_L values indicates that in *new_10*,

388   more grid points undergo an inhomogeneous mixing process, and the proportion of such

389   grid points is much larger than in the *new* model (Table 5). Therefore, compared to *new*,

390   *new_10* exhibit a smaller ψ and the effects of the new entrainment-mixing

391   parameterization on cloud properties are more obvious, for both the cumulus and

392   stratocumulus cases.

393

3.5 Verification by the simulations with a different parameterization using entrained air relative humidity

396   In the above simulations, the new entrainment-mixing parameterization is based

397   on the grid-mean RH. This section serves to verify these simulations using the the

398   entrainment-mixing parameterization proposed by Luo et al. (2020)

$$\psi = 107.96 \exp(-0.95 N_{\mathrm{L}}^{-0.35}), \tag{9}$$

400   which was developed using the entrained air RH in the EMPM. This parameterization

401   needs the entrained air RH within each grid in WRF, which is estimated following

402   Grabowski (2007) and Jarecka et al. (2009). Briefly, assuming that RH mixes linearly

403   when the dry air entrains into the cloud, then entrained air RH can be simply calculated

404   by

$$RH_{\mathrm{entrained}} = \frac{RH_{\mathrm{grid}} - (1-f)RH_{\mathrm{cloud}}}{f}, \tag{10}$$

406   where the subscripts *entrained*, *cloud*, and *grid* indicate the RH of the entrained, cloudy,

407   and grid point air, respectively. In Equation (10), although the cloudy air RH is

408   approximately 100% and grid-mean RH is predicted in the model, the entrained air

409   fraction f needs to be further parameterized. To obtain f at 100 m, a parameterization of

410   f is developed based on the simulations for both the cumulus and stratocumulus cases

411   with a higher resolution of 10 m; the other configurations are the same as those in the

412   experiment *default*. The 10 m-resolution simulation results are then averaged to the

413   resolution of 100 m. Following Xu and Randall (1996), "1 - f " can be fitted by the

414   function

$$1-f=RH_{\text{grid}}^{\gamma}\left[1-\exp\left(-\beta q_{\text{c}}\right)\right], \tag{11}$$

416   where γ and β are empirical parameters. Figure 8 shows that the parameterization with

417     $\gamma = 8.72$ and $\beta = 1.47\times10^{4}$ can well reproduce the simulated values of "$1 - f$", with the

418   correlation coefficient (R) of 0.89 and significant level p value < 0.01. Considering

419   that local shear ($\text{d}w/\text{d}z$) and buoyancy (B) may drive turbulence generation and

420   entrainment for a microscale process, the two quantities are also used to fit "$1 - f$"

421   except for RH_{grid} and q_{c}. However, the addition of $\text{d}w/\text{d}z$ and B to Equation (11) does

422   not increase R. Therefore, using RH_{grid} and q_{c} to parametrize "$1 - f$" is good and

423   reasonable for a microscale process.

424   Equations (9-11) are applied in the simulations for both the cumulus and

425   stratocumulus cases with different aerosol background (hereafter *new_f* and

426   *new_f_10*). Same as Figures 3 and 5, the temporal evolutions of the cloud physical

427   properties (q_{c}, N_{c}, r_{v}, CWP, and τ) in *default*, *default_10*, *new_f*, and *new_f_10* are

428   shown in Figures 9 and 10. The results are similar to Figures 3 and 5. The mean values

429   of these properties of *new_f* and *new_f_10* for the cumulus and stratocumulus cases

430   are also shown in Table 6, the results of *new* and *new_10* are also shown in the

431   parentheses for the convenience of comparison. The results of *new_f* and *new* are very

432   similar, with the maximum difference being no more than 1%, so are the results of

433   tenfold aerosol background. Such a close agreement suggests that the results of the

434   new entrainment-mixing parametrization with grid-mean RH are reliable.

435   It is worth noting that instead of parameterizing f, Jarecka et al. (2009) and

436   Jarecka et al. (2013) added an equation to predict f for each grid. In principle, this is a

437   good choice if this method is available in models. Our method shown here is an

438   alternative way to represent entrainment-mixing process when the prognostic f is not

439   available.

440

441   **4. Concluding remarks**

442   The entrainment-mixing process near cloud edges has important effects on cloud

443   microphysics, but the most commonly used microphysics schemes simply assume one

444   extreme mechanism, that is, homogeneous entrainment-mixing. This study first

445   improves the entrainment-mixing parameterization proposed by Luo et al. (2020),

446   which connects the homogeneous mixing degree and transition scale number to

447   estimate the homogeneity of the subgrid mixing process and its impact on the droplet

448   number concentration. The improved parameterization uses grid-mean relative

449   humidity and can be implemented directly into microphysics schemes; there is no need

450   to know the relative humidity of the entrained air. Second, the modified entrainment-

451   mixing parameterization is implemented in the two-moment Thompson aerosol-aware

452   scheme of the LES version of WRF-Solar, to examine its effects on the microphysical

453   and optical properties of cumulus and stratocumulus clouds. Third, several sensitivity

454   experiments are conducted to investigate the effects of the new entrainment-mixing

455   parameterization under different conditions of turbulence dissipation rate and aerosol

456 number concentration. The results of implementing the new entrainment-mixing

457 parameterization are finally verified by the results using entrained air properties.

458   Unlike the commonly assumed homogeneous mixing scenario, the new

459 entrainment-mixing parameterization produces a smaller cloud droplet number

460 concentration and larger cloud droplet radius, with the degree of difference depending

461 on cloud types and stages. Sensitivity tests show that in the cumulus case, the largest

462 average influence of the new entrainment-mixing parameterization occurs under a high

463 aerosol background, but results in only a 2.74% decrease in cloud droplet number

464 concentration and a 0.57% increase in cloud droplet volume-mean radius. The changes

465 become even smaller with a low aerosol background because of the larger cloud droplet

466 radius. In contrast, the new entrainment-mixing parameterization has a larger influence

467 on the microphysical and optical properties of stratocumulus clouds, especially under a

468 high aerosol background and during the mature stage, with a cloud fraction equal to 1.

469 The largest changes resulting from the new entrainment-mixing parameterization are –

470 9.69%, +3.88%, and –5.85%, for cloud number concentration, cloud droplet volume-

471 mean radius, and cloud optical depth, respectively. The new entrainment-mixing

472 parameterization has less of an influence on the dissipation stage than on the mature

473 stage of the stratocumulus case, but affects this case more than the cumulus case.

474   The varying effects of the new entrainment-mixing parameterization are caused

475 by variations in the dominant entrainment-mixing mechanism between different cloud

476 types and stages. Compared to the cumulus case, the stratocumulus case has a much

477   smaller homogeneous mixing degree and a larger proportion of inhomogeneous mixing

478   grid points, especially during the mature stage, which indicates that the inhomogeneous

479   mixing mechanism dominates in the stratocumulus case, while the homogeneous

480   mixing mechanism dominates in the cumulus case. As mentioned above, the changes

481   in physical properties of stratocumulus clouds in the dissipation stage are between those

482   in the mature stage and those of the cumulus case; this is because stratocumulus clouds

483   dissipate sharply to form small cumulus clouds, and the degree of homogeneous mixing

484   during the dissipation stage is therefore between that which occurs during the mature

485   stage and the cumulus case.

486   Sensitivity studies show that turbulence dissipation rate and aerosol concentration

487   can have notable effects on the subgrid homogeneity of the mixing process. A larger

488   dissipation rate can accelerate the mixing process, which results in a larger transition

489   scale number and homogeneous mixing degree; and therefore, a mostly homogenous

490   mixing mechanism. This is why the cumulus case exhibit smaller changes than the

491   stratocumulus case after the new entrainment-mixing parameterization is implemented.

492   Larger aerosol number concentrations cause a smaller cloud droplet radius. Smaller

493   droplets evaporate more easily, which leads to a smaller transition scale number and a

494   smaller homogeneous mixing degree. Thus, the entrainment-mixing mechanism tends

495   to be inhomogeneous. Therefore, a larger aerosol number concentration increases the

496   influence of the new entrainment-mixing parameterization in both the cumulus and

497   stratocumulus cases.

498   The influences of implementing the new entrainment-mixing parameterization

499   with grid-mean relative humidity have been verified by simulations with entrained air

500   properties. The entrained air properties are obtained and calculated from simulations

501   with a finer resolution (10 m). Sensitivity tests show similar cloud microphysical and

502   optical properties in the two different methods, which suggests that the new

503   entrainment-mixing parameterization with grid-mean relative humidity is convincing.

504   Note that the new entrainment-mixing parameterization could be more important

505   in the models if the relative humidity near the cloud is more accurately simulated,

506   because numerical diffusion may spuriously humidify the entrained air (Hoffmann and

507   Feingold, 2019). The artificially increased relative humidity limits the influences of the

508   new entrainment-mixing parameterization, because homogeneous and inhomogeneous

509   entrainment-mixing processes are close to each other under conditions of high relative

510   humidity.

511

512   **Author contributions.** XX, CL and YL designed the experiments. XX carried out the

513   experiments and conducted the data analysis with contributions from all coauthors. XX,

514   CL, XZ, and SE developed the model code. XX prepared the paper with help from CL,

515   YL, YW, SL, and LZ.

516

517   **Competing interests.** The authors declare that they have no conflict of interest.

518

Acknowledgements. This research is supported by the National Key Research and

Development Program of China (2017YFA0604001), the National Natural Science

Foundation of China (41822504, 42175099, 42027804, 41975181, 42075073). Liu,

Zhou, and Endo are supported by the U.S. Department of Energy's Office of Energy

Efficiency and Renewable Energy (EERE) under Solar Energy Technologies Office

(SETO) Award Number 33504, and Office of Science Biological and Environmental

Research as part of the Atmospheric Systems Research (ASR) Program. Brookhaven

National Laboratory is operated by Battelle for the U.S. Department of Energy under

Contract DE-SC00112704. The large-scale forcing data used in this paper can be

downloaded from the U.S. Department of Energy's Atmospheric Radiation

Measurement Program with https://adc.arm.gov/discovery/#/results. The LASSO data

can be downloaded from https://archive.arm.gov/lassobrowser. The views expressed

herein do not necessarily represent the views of the U.S. Department of Energy or the

United States Government.

Reference

Ackerman, A. S., Kirkpatrick, M. P., Stevens, D. E., and Toon, O. B.: The impact of humidity above stratiform clouds on indirect aerosol climate forcing, Nature, 432, 1014-1017, 2004.

Andrejczuk, M., Grabowski, W. W., Malinowski, S. P., and Smolarkiewicz, P. K.: Numerical simulation of cloud-clear air interfacial mixing: Effects on cloud microphysics, J. Atmos. Sci., 63, 3204-3225, doi:10.1175/JAS3813.1, 2006.

Andrejczuk, M., Grabowski, W. W., Malinowski, S. P., and Smolarkiewicz, P. K.: Numerical simulation of cloud–clear air interfacial mixing: Homogeneous versus inhomogeneous mixing, J. Atmos. Sci., 66, 2493-2500, doi:10.1175/2009JAS2956.1, 2009.

545 Burnet, F. and Brenguier, J. L.: Observational study of the entrainment-mixing process
546 in warm convective clouds, J. Atmos. Sci., 64, 1995-2011, doi:10.1175/JAS3928.1,
547 2007.

548 Chosson, F., Brenguier, J.-L., and Schüller, L.: Entrainment-mixing and radiative
549 transfer simulation in boundary layer clouds, J. Atmos. Sci., 64, 2670-2682,
550 doi:10.1175/JAS3975.1, 2007.

551 Deardorff, J.: Stratocumulus-capped mixed layers derived from a three-dimensional
552 model, Boundary-Layer Meteorol, 18, 495-527, 10.1007/BF00119502, 1980.

553 Del Genio, A. D. and Wu, J.: The role of entrainment in the diurnal cycle of continental
554 convection, J. Climate, 23, 2722-2738, doi: 10.1175/2009JCLI3340.1, 2010.

555 Endo, S., Fridlind, A. M., Lin, W., Vogelmann, A. M., Toto, T., Ackerman, A. S.,
556 McFarquhar, G. M., Jackson, R. C., Jonsson, H. H., and Liu, Y.: RACORO continental
557 boundary layer cloud investigations: 2. Large‐eddy simulations of cumulus clouds
558 and evaluation with in situ and ground‐based observations, Journal of Geophysical
559 Research: Atmospheres, 120, 5993-6014, 2015.

560 Fan, J., Wang, Y., Rosenfeld, D., and Liu, X.: Review of Aerosol–Cloud Interactions:
561 Mechanisms, Significance, and Challenges, Journal of the Atmospheric Sciences, 73,
562 4221-4252, 10.1175/jas-d-16-0037.1, 2016.

563 Freud, E., Rosenfeld, D., and Kulkarni, J. R.: Resolving both entrainment-mixing and
564 number of activated CCN in deep convective clouds, Atmos. Chem. Phys., 11, 12887-
565 12900, 2011.

566 Freud, E., Rosenfeld, D., Andreae, M. O., Costa, A. A., and Artaxo, P.: Robust relations
567 between CCN and the vertical evolution of cloud drop size distribution in deep
568 convective clouds, Atmos. Chem. Phys., 8, 1661-1675, 2008.

569 Gao, S., Lu, C., Liu, Y., Mei, F., Wang, J., Zhu, L., and Yan, S.: Contrasting Scale
570 Dependence of Entrainment‐Mixing Mechanisms in Stratocumulus Clouds,
571 Geophysical Research Letters, 47, 10.1029/2020gl086970, 2020.

572 Gao, S., Lu, C., Liu, Y., Yum, S. S., Zhu, J., Zhu, L., Desai, N., Ma, Y., and Wu, S.:
573 Comprehensive quantification of height dependence of entrainment mixing between
574 stratiform cloud top and environment, Atmospheric Chemistry and Physics, 21, 11225-
575 11241, 2021.

576 Gao, Z., Liu, Y., Li, X., and Lu, C.: Investigation of Turbulent Entrainment-Mixing
577 Processes with a New Particle-Resolved Direct Numerical Simulation Model, J.
578 Geophys. Res., 123, 2194-2214, 2018.

579 Gerber, H. E., Frick, G. M., Jensen, J. B., and Hudson, J. G.: Entrainment, mixing, and
580 microphysics in trade-wind cumulus, J. Meteorol. Soc. Japan, 86A, 87-106, 2008.

581 Grabowski, W. W.: Indirect impact of atmospheric aerosols in idealized simulations of
582 convective-radiative quasi equilibrium, J. Climate, 19, 4664-4682,
583 doi:10.1175/JCLI3857.1, 2006.

584 Grabowski, W. W.: Representation of turbulent mixing and buoyancy reversal in bulk
585 cloud models, Journal of the atmospheric sciences, 64, 3666-3680, 2007.

586 Grabowski, W. W. and Morrison, H.: Indirect Impact of Atmospheric Aerosols in

Idealized Simulations of Convective–Radiative Quasi Equilibrium. Part II: Double-Moment Microphysics, Journal of Climate, 24, 1897-1912, 10.1175/2010jcli3647.1, 2011.

Gustafson, W. I., Vogelmann, A. M., Li, Z., Cheng, X., Dumas, K. K., Endo, S., Johnson, K. L., Krishna, B., Fairless, T., and Xiao, H.: The Large-Eddy Simulation (LES) Atmospheric Radiation Measurement (ARM) Symbiotic Simulation and Observation (LASSO) Activity for Continental Shallow Convection, Bulletin of the American Meteorological Society, 101, E462-E479, 10.1175/bams-d-19-0065.1, 2020.

Hacker, J. P., Jimenez, P. A., Dudhia, J., Haupt, S. E., Ruiz-Arias, J. A., Gueymard, C. A., Thompson, G., Eidhammer, T., and Deng, A.: WRF-Solar: Description and Clear-Sky Assessment of an Augmented NWP Model for Solar Power Prediction, Bulletin of the American Meteorological Society, 97, 1249-1264, 10.1175/bams-d-14-00279.1, 2016.

Haman, K. E., Malinowski, S. P., Kurowski, M. J., Gerber, H., and Brenguier, J.-L.: Small scale mixing processes at the top of a marine stratocumulus - a case study, Q. J. Roy. Meteor. Soc., 133, 213-226, doi:10.1002/qj.5, 2007.

Haupt, S. E., Kosovic, B., Jensen, T., Lee, J., Jimenez, P., Lazo, J., Cowie, J., McCandless, T., Pearson, J., and Weiner, G.: The SunCast☐ solar-power forecasting system: the results of the public-private-academic partnership to advance solar power forecasting, National Center for Atmospheric Research (NCAR), Boulder (CO): Research Applications Laboratory, Weather Systems and Assessment Program (US), 2016.

Hill, A. A., Feingold, G., and Jiang, H.: The influence of entrainment and mixing assumption on aerosol-cloud interactions in marine stratocumulus, J. Atmos. Sci., 66, 1450-1464, 2009.

Hoffmann, F. and Feingold, G.: Entrainment and mixing in stratocumulus: Effects of a new explicit subgrid-scale scheme for large-eddy simulations with particle-based microphysics, J. Atmos. SCi., 76, 1955-1973, 10.1175/jas-d-18-0318.1, 2019.

Hoffmann, F., Yamaguchi, T., and Feingold, G.: Inhomogeneous mixing in Lagrangian cloud models: Effects on the production of precipitation embryos, Journal of the Atmospheric Sciences, 76, 113-133, 2019.

Huang, J., Lee, X., and Patton, E. G.: A modelling study of flux imbalance and the influence of entrainment in the convective boundary layer, Boundary-layer meteorology, 127, 273-292, 2008.

Jarecka, D., Grabowski, W. W., and Pawlowska, H.: Modeling of Subgrid-Scale Mixing in Large-Eddy Simulation of Shallow Convection, Journal of the Atmospheric Sciences, 66, 2125-2133, 10.1175/2009jas2929.1, 2009.

Jarecka, D., Grabowski, W. W., Morrison, H., and Pawlowska, H.: Homogeneity of the subgrid-scale turbulent mixing in large-eddy simulation of shallow convection, J. Atmos. Sci., 70, 2751-2767, 2013.

Jensen, J. B., Austin, P. H., Baker, M. B., and Blyth, A. M.: Turbulent mixing, spectral evolution and dynamics in a warm cumulus cloud, J. Atmos. Sci., 42, 173-192,

629 doi:10.1175/1520-0469(1985)042<0173:TMSEAD>2.0.CO;2, 1985.

630 Kim, B.-G., Miller, M. A., Schwartz, S. E., Liu, Y., and Min, Q.: The role of adiabaticity
631 in the aerosol first indirect effect, J. Geophys. Res., 113, D05210, doi:
632 10.1029/2007jd008961, 2008.

633 Kumar, B., Schumacher, J., and Shaw, R.: Cloud microphysical effects of turbulent
634 mixing and entrainment, Theor. Comp. Fluid Dyn., 27, 361-376, 2013.

635 Lasher-Trapp, S. G., Cooper, W. A., and Blyth, A. M.: Broadening of droplet size
636 distributions from entrainment and mixing in a cumulus cloud, Q. J. Roy. Meteor. Soc.,
637 131, 195-220, doi:10.1256/qj.03.199, 2005.

638 Lehmann, K., Siebert, H., and Shaw, R. A.: Homogeneous and inhomogeneous mixing
639 in cumulus clouds: dependence on local turbulence structure, J. Atmos. Sci., 66, 3641-
640 3659, doi:10.1175/2009JAS3012.1, 2009.

641 Li, Z., Li, C., Chen, H., Tsay, S. C., Holben, B., Huang, J., Li, B., Maring, H., Qian, Y.,
642 and Shi, G.: East Asian studies of tropospheric aerosols and their impact on regional
643 climate (EAST‐AIRC): An overview, Journal of Geophysical Research: Atmospheres,
644 116, 2011.

645 Lu, C., Liu, Y., and Niu, S.: Examination of turbulent entrainment-mixing mechanisms
646 using a combined approach, J. Geophys. Res., 116, D20207,
647 doi:10.1029/2011JD015944, 2011.

648 Lu, C., Liu, Y., Niu, S., and Endo, S.: Scale dependence of entrainment‐mixing
649 mechanisms in cumulus clouds, Journal of Geophysical Research: Atmospheres, 119,
650 13,877-813,890, 2014.

651 Lu, C., Liu, Y., Niu, S., Krueger, S., and Wagner, T.: Exploring parameterization for
652 turbulent entrainment-mixing processes in clouds, Journal of Geophysical Research:
653 Atmospheres, 118, 185-194, 10.1029/2012jd018464, 2013.

654 Lu, C., Liu, Y., Zhang, G. J., Wu, X., Endo, S., Cao, L., Li, Y., and Guo, X.: Improving
655 parameterization of entrainment rate for shallow convection with aircraft measurements
656 and large eddy simulation, J. Atmos. Sci., 73, 761-773, 10.1175/JAS-D-15-0050.1,
657 2016.

658 Luo, S., Lu, C., Liu, Y., Bian, J., Gao, W., Li, J., Xu, X., Gao, S., Yang, S., and Guo, X.:
659 Parameterizations of Entrainment‐Mixing Mechanisms and Their Effects on Cloud
660 Droplet Spectral Width Based on Numerical Simulations, Journal of Geophysical
661 Research: Atmospheres, 125, e2020JD032972, 2020.

662 Morrison, H. and Grabowski, W. W.: Modeling supersaturation and subgrid-scale
663 mixing with two-moment bulk warm microphysics, J. Atmos. Sci., 65, 792-812,
664 doi:10.1175/2007JAS2374.1, 2008.

665 Paluch, I. R. and Baumgardner, D. G.: Entrainment and fine-scale mixing in a
666 continental convective cloud, J. Atmos. Sci., 46, 261-278, doi:10.1175/1520-
667 0469(1989)046<0261:EAFSMI>2.0.CO;2, 1989.

668 Pawlowska, H., Brenguier, J. L., and Burnet, F.: Microphysical properties of
669 stratocumulus clouds, Atmos. Res., 55, 15-33, 2000.

670 Peng, Y., Lohmann, U., Leaitch, R., Banic, C., and Couture, M.: The cloud albedo-cloud

671 droplet effective radius relationship for clean and polluted clouds from RACE and
672 FIRE.ACE, J. Geophys. Res., 107, AAC 1-1-AAC 1-6, 10.1029/2000JD000281, 2002.
673 Slawinska, J., Grabowski, W. W., Pawlowska, H., and Morrison, H.: Droplet activation
674 and mixing in large-eddy simulation of a shallow cumulus field, J. Atmos. Sci., 69, 444-
675 462, 2012.
676 Slawinska, J., Grabowski, W. W., Pawlowska, H., and Wyszogrodzki, A. A.: Optical
677 properties of shallow convective clouds diagnosed from a bulk-microphysics large-
678 eddy simulation, J. Climate, 21, 1639-1647, 2008.
679 Small, J. D., Chuang, P., and Jonsson, H.: Microphysical imprint of entrainment in
680 warm cumulus, Tellus B, 65, 6647-6662, 2013.
681 Thompson, G. and Eidhammer, T.: A study of aerosol impacts on clouds and
682 precipitation development in a large winter cyclone, Journal of the atmospheric
683 sciences, 71, 3636-3658, 2014.
684 Wang, H. and Feingold, G.: Modeling mesoscale cellular structures and drizzle in
685 marine stratocumulus. Part I: Impact of drizzle on the formation and evolution of open
686 cells, Journal of the Atmospheric Sciences, 66, 3237-3256, 2009.
687 Wang, M., Ghan, S., Ovchinnikov, M., Liu, X., Easter, R., Kassianov, E., Qian, Y., and
688 Morrison, H.: Aerosol indirect effects in a multi-scale aerosol-climate model PNNL-
689 MMF, Atmospheric Chemistry and Physics, 11, 5431-5455, 2011.
690 Wang, Y., Zhao, C., McFarquhar, G. M., Wu, W., Reeves, M., and Li, J.: Dispersion of
691 Droplet Size Distributions in Supercooled Non‐precipitating Stratocumulus from
692 Aircraft Observations Obtained during the Southern Ocean Cloud Radiation Aerosol
693 Transport Experimental Study, Journal of Geophysical Research: Atmospheres, 126,
694 e2020JD033720, 2021.
695 Wang, Y., Niu, S., Lv, J., Lu, C., Xu, X., Wang, Y., Ding, J., Zhang, H., Wang, T., and
696 Kang, B.: A new method for distinguishing unactivated particles in cloud condensation
697 nuclei measurements: Implications for aerosol indirect effect evaluation, Geophysical
698 Research Letters, 46, 14185-14194, 2019.
699 Wood, R.: Review: Stratocumulus Clouds, Monthly Weather Review, 140, 2373-2423,
700 2012.
701 Xu, K.-M. and Randall, D. A.: A semiempirical cloudiness parameterization for use in
702 climate models, Journal of the atmospheric sciences, 53, 3084-3102, 1996.
703 Xu, X., Sun, C., Lu, C., Liu, Y., Zhang, G. J., and Chen, Q.: Factors affecting
704 entrainment rate in deep convective clouds and parameterizations, Journal of
705 Geophysical Research: Atmospheres, 126, e2021JD034881, 2021.
706 Xu, X., Lu, C., Liu, Y., Gao, W., Wang, Y., Cheng, Y., Luo, S., and Van Weverberg, K.:
707 Effects of cloud liquid‐phase microphysical processes in mixed‐phase cumuli over
708 the Tibetan Plateau, Journal of Geophysical Research: Atmospheres, 125,
709 e2020JD033371, 2020.
710 Yang, B., Wang, M., Zhang, G. J., Guo, Z., Huang, A., Zhang, Y., and Qian, Y.: Linking
711 Deep and Shallow Convective Mass Fluxes via an Assumed Entrainment Distribution
712 in CAM5‐CLUBB: Parameterization and Simulated Precipitation Variability, Journal

713   of Advances in Modeling Earth Systems, 13, e2020MS002357, 2021.

714   Yang, F., Shaw, R., and Xue, H.: Conditions for super-adiabatic droplet growth after

715   entrainment mixing, Atmos. Chem. Phys., 16, 9421-9433, 10.5194/acp-2016-94, 2016.

716   Yum, S.: Cloud droplet spectral broadening in warm clouds: An observational and

717   model study, Dissertation for the Doctoral Degree, University of Nevada, Reno, Nevada,

718   USA, 191 pp., 1998.

719   Zhang, M. H., Lin, J. L., Cederwall, R. T., Yio, J. J., and Xie, S. C.: Objective analysis

720   of ARM IOP data: Method and sensitivity, Mon. Weather Rev., 129, 295-311,

721   10.1175/1520-0493(2001)129<0295:OAOAID>2.0.CO;2, 2001.

722   Zheng, Y. and Rosenfeld, D.: Linear relation between convective cloud base height and

723   updrafts and application to satellite retrievals, Geophysical Research Letters, 42, 6485-

724   6491, 10.1002/2015gl064809, 2015.

725   Zheng, Y., Rosenfeld, D., and Li, Z.: Quantifying cloud base updraft speeds of marine

726   stratocumulus from cloud top radiative cooling, Geophysical Research Letters, 43,

727   11,407-411,413, 2016.

728   Zhu, L., Lu, C., Yan, S., Liu, Y., Zhang, G. J., Mei, F., Zhu, B., Fast, J. D., Matthews,

729   A., and Pekour, M. S.: A New Approach for Simultaneous Estimation of Entrainment

730   and Detrainment Rates in Non‐Precipitating Shallow Cumulus, Geophysical Research

731   Letters, 48, 10.1029/2021gl093817, 2021.

732

733

734   Table 1. Summary of names and corresponding descriptions of the four experiments for

735   each case of cumulus and stratocumulus. The meaning of each symbol for each

736   experiment can be found in the text.

	Entrainment-mixing parameterization	Dissipation rate	Aerosol number concentration
default	$\alpha = 0$	-	default
new	$\alpha = 1 - \psi,$ $\psi = 107.19\exp(-1.99N_{\mathrm{L}}^{-0.29}).$	$\varepsilon = CE^{3/2} / L.$	default
default_10	$\alpha = 0$	-	default×10
new_10	$\alpha = 1 - \psi,$ $\psi = 107.19\exp(-1.99N_{\mathrm{L}}^{-0.29}).$	$\varepsilon = CE^{3/2} / L.$	default×10

737

738   Table 2. Summary of the case mean values of the key quantities in all the simulations

739   of the cumulus case, containing cloud water mixing ratio (q_c), cloud droplet number

740   concentration (N_c), cloud droplet volume-mean radius (r_v), cloud water path (CWP),

741   and cloud optical depth (τ). The experiments are detailed in Table 1.

	default	*new*	*default_10*	*new_10*
q_c(g/kg)	0.44	0.44	0.56	0.57
N_c(cm^{-3})	35.78	35.53	278.80	271.16
r_v(μm)	13.27	13.29	7.05	7.09
CWP(g/m^2)	142.30	144.25	186.52	187.13
τ	13.07	13.02	31.29	31.11

742

743

744 Table 3. Summary of the case mean values of the key quantities in all the simulations

745 of the stratocumulus case, including cloud water mixing ratio (q_c), cloud droplet number

746 concentration (N_c), cloud droplet volume-mean radius (r_v), cloud water path (CWP),

747 and cloud optical depth (τ). The numbers in and out of the parentheses are the results at

748 the mature and dissipation stages, respectively. The experiments are detailed in Table 1.

	default	*new*	*default_10*	*new_10*
q_c(g/kg)	0.13	0.13	0.16	0.16
	(0.039)	(0.039)	(0.041)	(0.041)
N_c(cm^{-3})	35.74	33.11	256.82	231.93
	(19.76)	(18.82)	(138.74)	(126.90)
r_v(μm)	10.32	10.65	5.15	5.35
	(7.53)	(7.69)	(4.02)	(4.14)
CWP(g/m^2)	41.39	41.78	56.21	57.03
	(2.57)	(2.43)	(2.71)	(2.77)
τ	4.68	4.40	13.17	12.40
	(0.39)	(0.38)	(0.78)	(0.78)

749

750 Table 4. Cloud water mixing ratio (q_c), cloud droplet number concentration (N_c), cloud

751 droplet volume-mean radius (r_v), cloud water path (CWP), cloud optical depth (τ) in all

752 simulations for the entire lifetime of the stratocumulus case. The experiments are

753 detailed in Table 1.

	default	*new*	*default_10*	*new_10*
q_c(g/kg)	0.11	0.11	0.13	0.13
N_c(cm^{-3})	29.98	28.12	223.65	203.50
r_v(μm)	9.38	9.57	5.06	5.22
CWP(g/m^2)	30.78	29.92	42.22	43.13
τ	4.02	3.89	10.39	9.96

754

755

756 Table 5. Homogeneous mixing degree (ψ) at all grid points experiencing evaporation,

757 the proportion of inhomogeneous mixing grid points to all grid points experiencing

758 evaporation, and ψ at the inhomogeneous mixing grid points in the experiments *new*

759 and *new_10* (Table 1) for the cumulus (Cu) and stratocumulus (St) cases. The numbers

760 in and out of the parentheses are the results at the mature and dissipation stages in the

761 stratocumulus (St) case, respectively. The experiments are detailed in Table 1.

	ψ at all grids (%)	Proportion of inhomogeneous mixing grids (%)	ψ at the inhomogeneous mixing grids (%)
new (Cu)	99.93	4.52	98.62
new_10 (Cu)	95.33	25.10	92.96
new (St)	78.56	63.07	71.56
	(94.68)	(40.61)	(89.33)
new_10 (St)	68.20	97.31	65.01
	(88.11)	(73.54)	(84.99)

762

763

764 Table 6. Cloud water mixing ratio (q_c), cloud droplet number concentration (N_c), cloud

765 droplet volume-mean radius (r_v), cloud water path (CWP), cloud optical depth (τ) in

766 *new_f* and *new_f_10* for the cumulus (Cu) and stratocumulus (Sc) cases. The results of

767 *new* and *new_10* in Tables 2 and 4 are shown in the parentheses.

	Cu		Sc	
	new_f	*new_f_10*	*new_f*	*new_f_10*
	(*new*)	(*new_10*)	(*new*)	(*new_10*)
q_c(g/kg)	0.44	0.57	0.11	0.13
	(0.44)	(0.57)	(0.11)	(0.13)
N_c(cm^{-3})	35.52	270.56	28.08	202.99
	(35.53)	(271.16)	(28.12)	(203.50)
r_v(μm)	13.30	7.10	9.60	5.21
	(13.29)	(7.09)	(9.57)	(5.22)
CWP(g/m^2)	143.15	185.95	30.16	43.32
	(144.25)	(187.13)	(29.92)	(43.13)
τ	13.00	31.08	3.89	9.93
	(13.02)	(31.11)	(3.89)	(9.96)

768

769

770
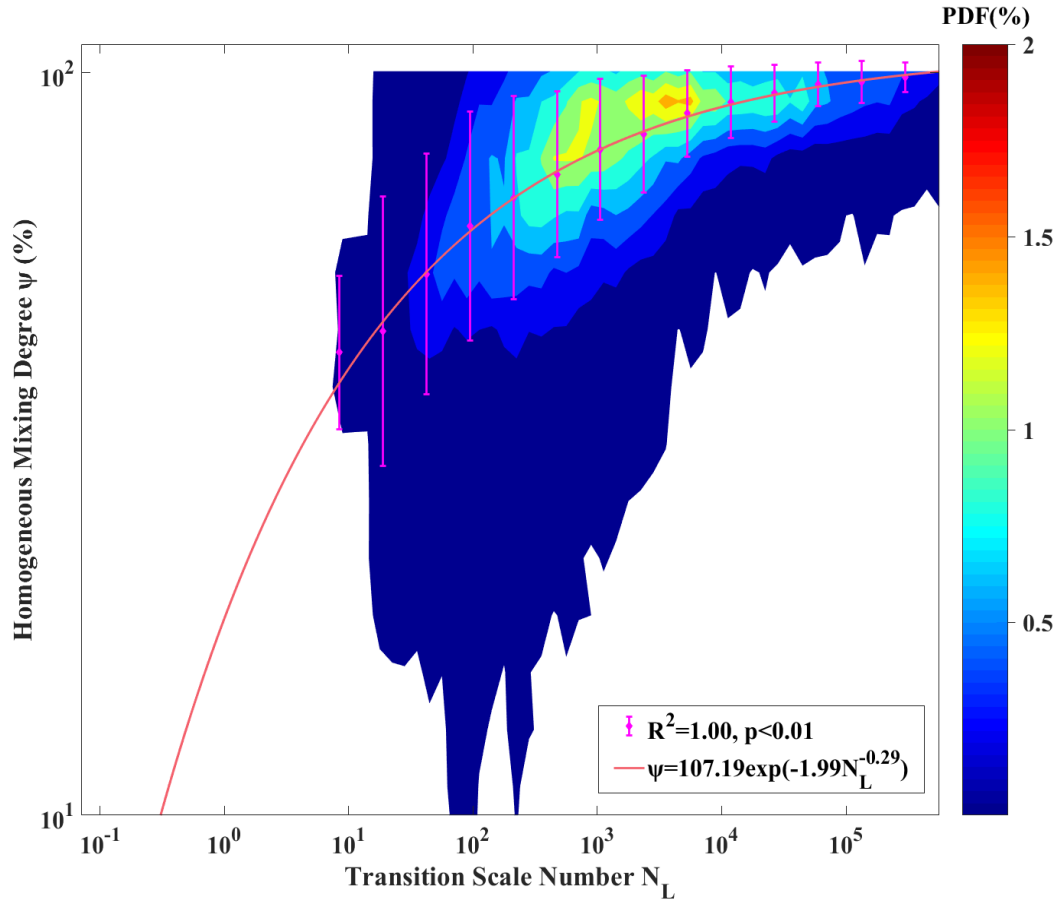
771 Figure 1. Parameterization of cloud entrainment-mixing mechanisms by relating

772 homogeneous mixing degree (ψ) to transition scale number (N_L) from EMPM. The

773 contours represent the joint probability distribution function (PDF) of ψ vs N_L. The

774 magenta dots and error bars are mean values and standard deviations of ψ in each N_L

775 bin, respectively. The mean values are fitted using a weighted least squares method with

776 the number of data points in each N_L bin as the weight. The fitting equation, coefficient

777 of determination (R^2), and p-value are also given. N_L is calculated by with the domain-

778 averaged relative humidity after entrainment but before evaporation in the EMPM.
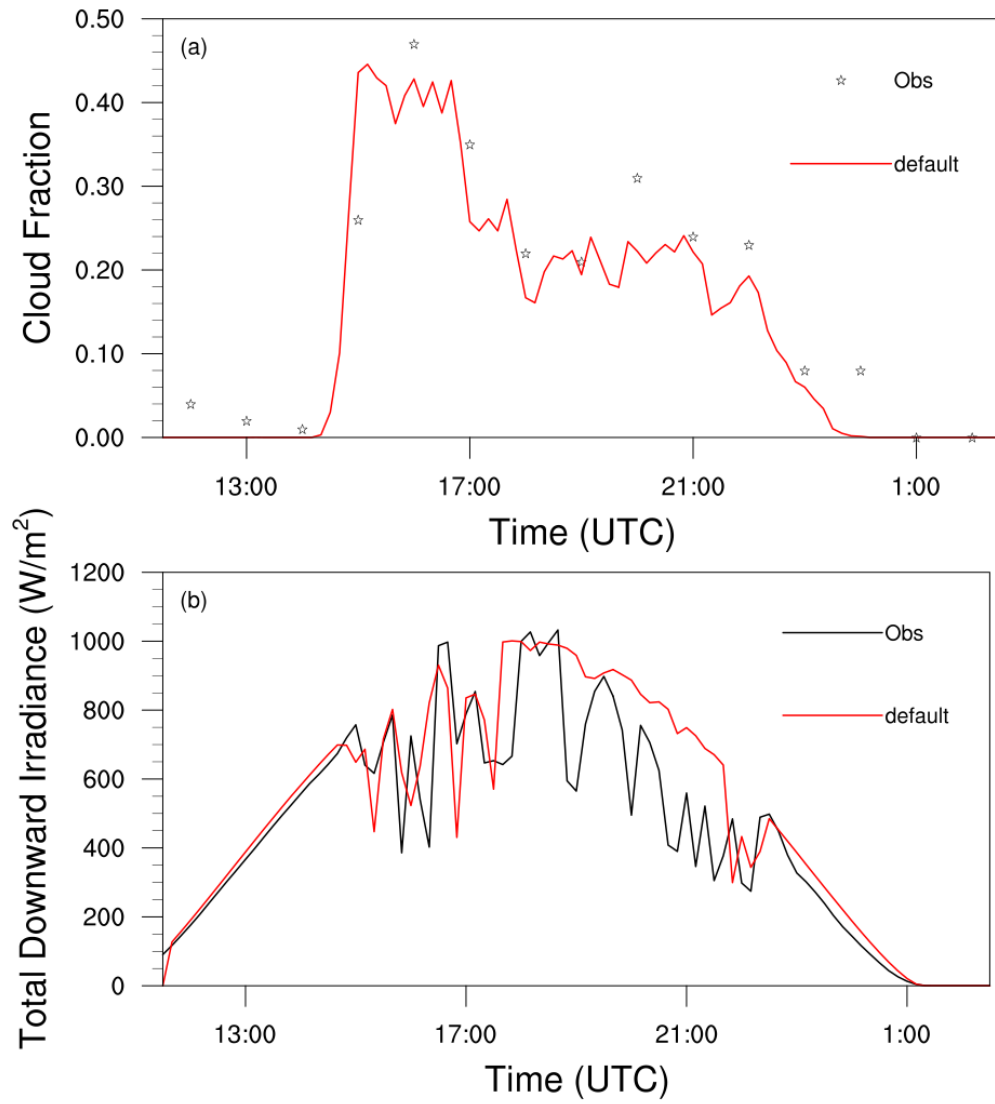
779

780 Figure 2. Time series of (a) domain-averaged cloud fraction and (b) total downward

781 irradiance at the central point from the observation and the *default* experiment in the

782 cumulus case.

783
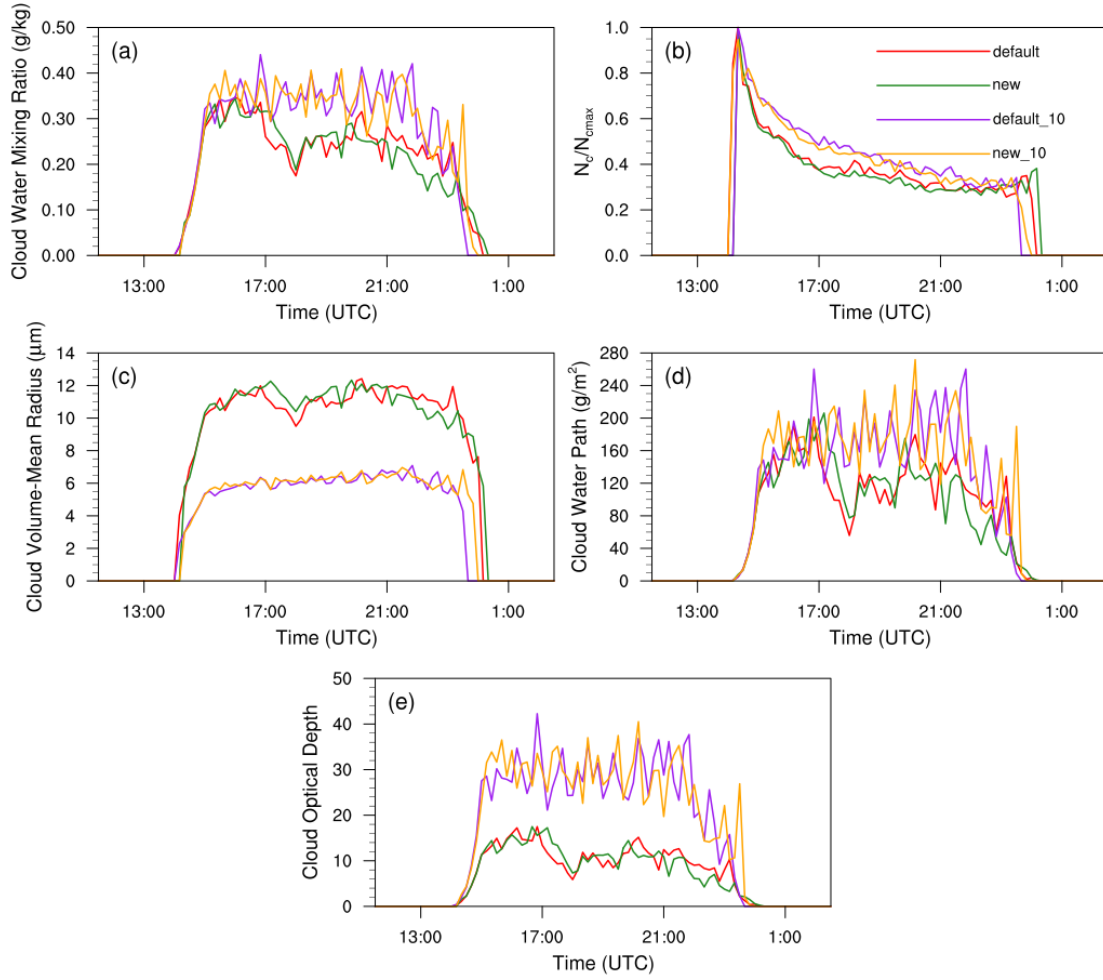
784

785 Figure 3. The temporal evolutions of main cloud microphysical and optical properties

786 in all simulation experiments for the cumulus case, including (a) cloud water mixing

787 ratio (q_c) (g/kg), (b) cloud droplet number concentration (N_c) (/cm^3), (c) cloud droplet

788 volume-mean radius (r_v) (μm), (d) cloud water path (CWP) (g/m^2), and (e) cloud optical

789 depth (τ). In (b), N_c in the experiments *default* and *new* are normalized by the maximum

790 cloud droplet concentration (N_{cmax}) from *default*, respectively; N_c in the experiments

791 *default_10* and *new_10* are normalized by N_{cmax} from *default_10*, respectively. The four

792 experiments are detailed in Table 1.
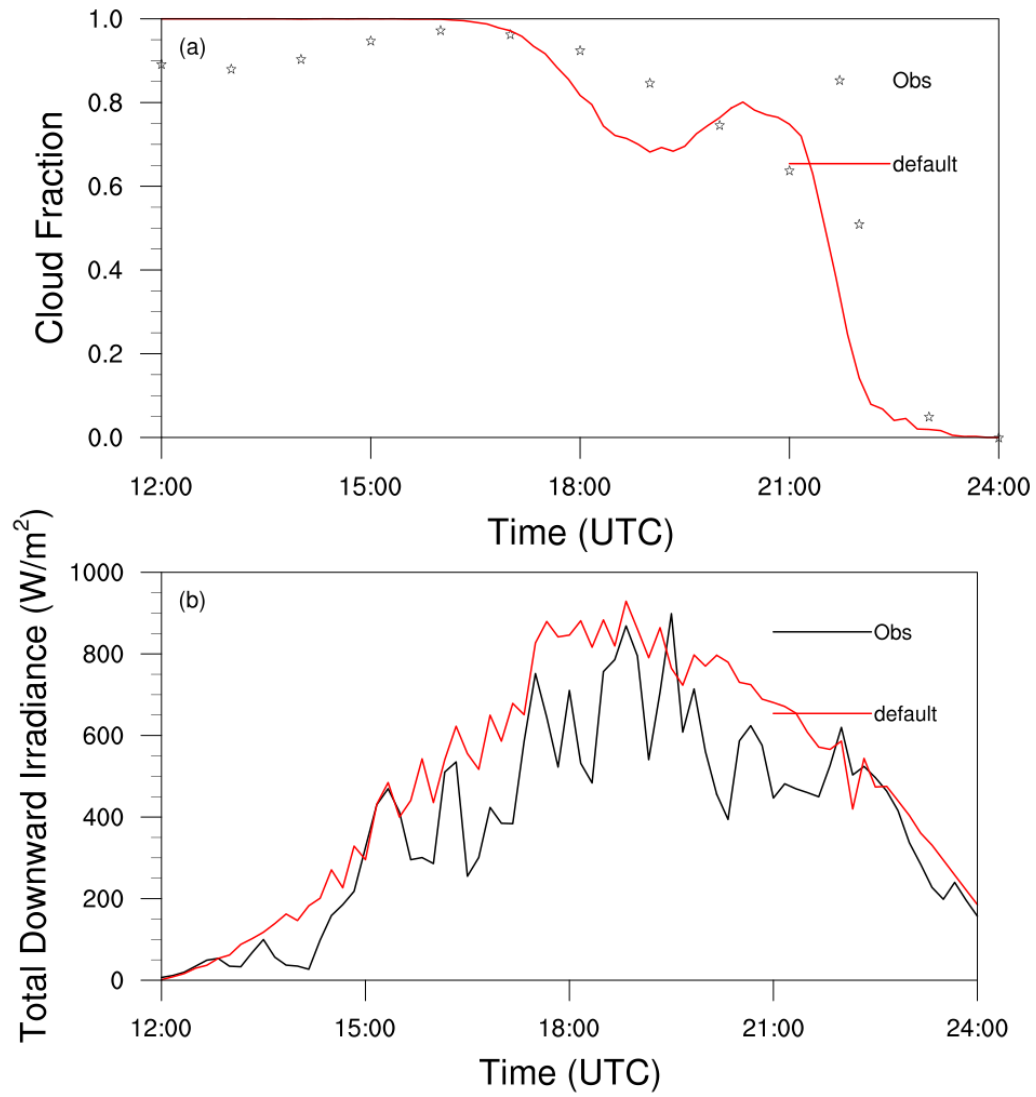
793

794   Figure 4. Time series of (a) domain-averaged cloud fraction and (b) total downward

795   irradiance at the central point from the observation and the *default* experiment in the

796   stratocumulus case.

797
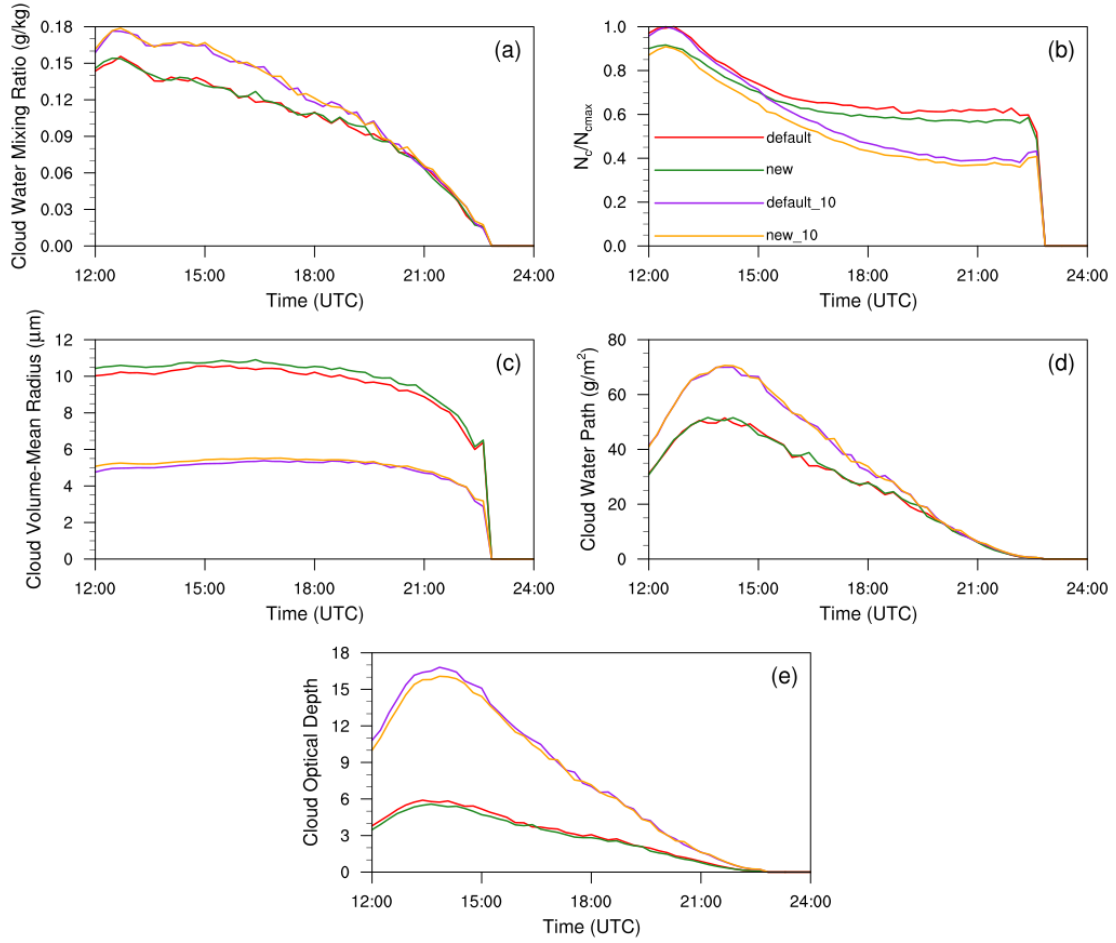
Figure 5. The temporal evolutions of main cloud microphysical and optical properties

in all simulation experiments for the stratocumulus case, including (a) cloud water

mixing ratio (q_c) (g/kg), (b) cloud droplet number concentration (N_c) (/cm^3), (c) cloud

droplet volume-mean radius (r_v) (μm), (d) cloud water path (CWP) (g/m^2), and (e) cloud

optical depth (τ). In (b), N_c in the experiments *default* and *new* are normalized by the

maximum cloud droplet number concentration (N_{cmax}) from *default*, respectively; N_c in

the experiments *default_10* and *new_10* are normalized by N_{cmax} from *default_10*,

respectively. The four experiments are detailed in Table 1.

806
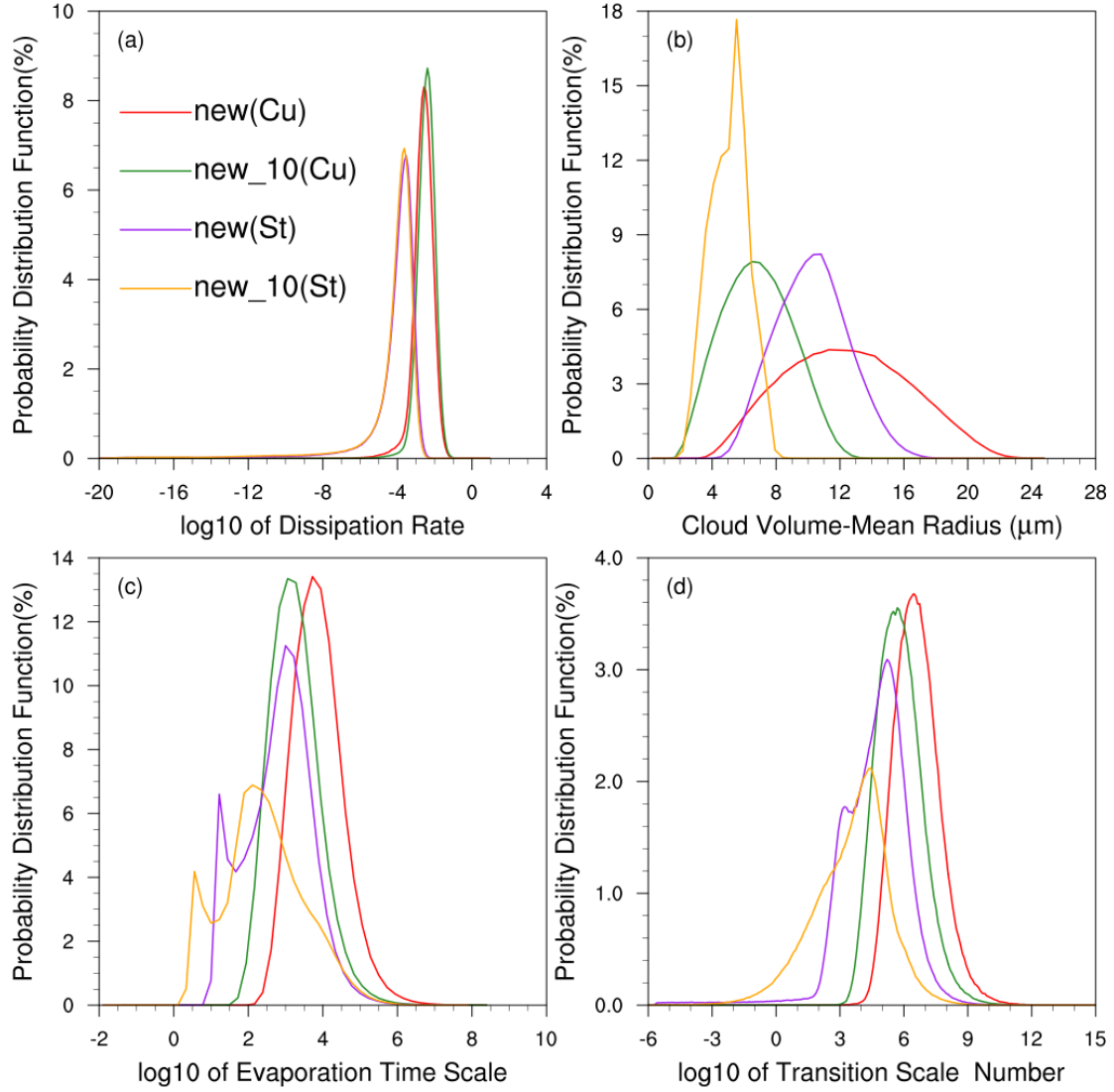
807 Figure 6. Probability distribution functions (PDFs) of (a) turbulence dissipation rate (ε),

808 (b) cloud droplet volume-mean radius (r_v), (c) evaporation time scale (τ_{evap}), and (d)

809 transition scale number (N_L) of cloud grids experiencing the entrainment-mixing

810 process in the simulations with the new entrainment-mixing parameterization for the

811 cumulus case (Cu, the solid lines) and the stratocumulus case (St, the dash lines),

812 respectively. The experiments are detailed in Table 1.

813
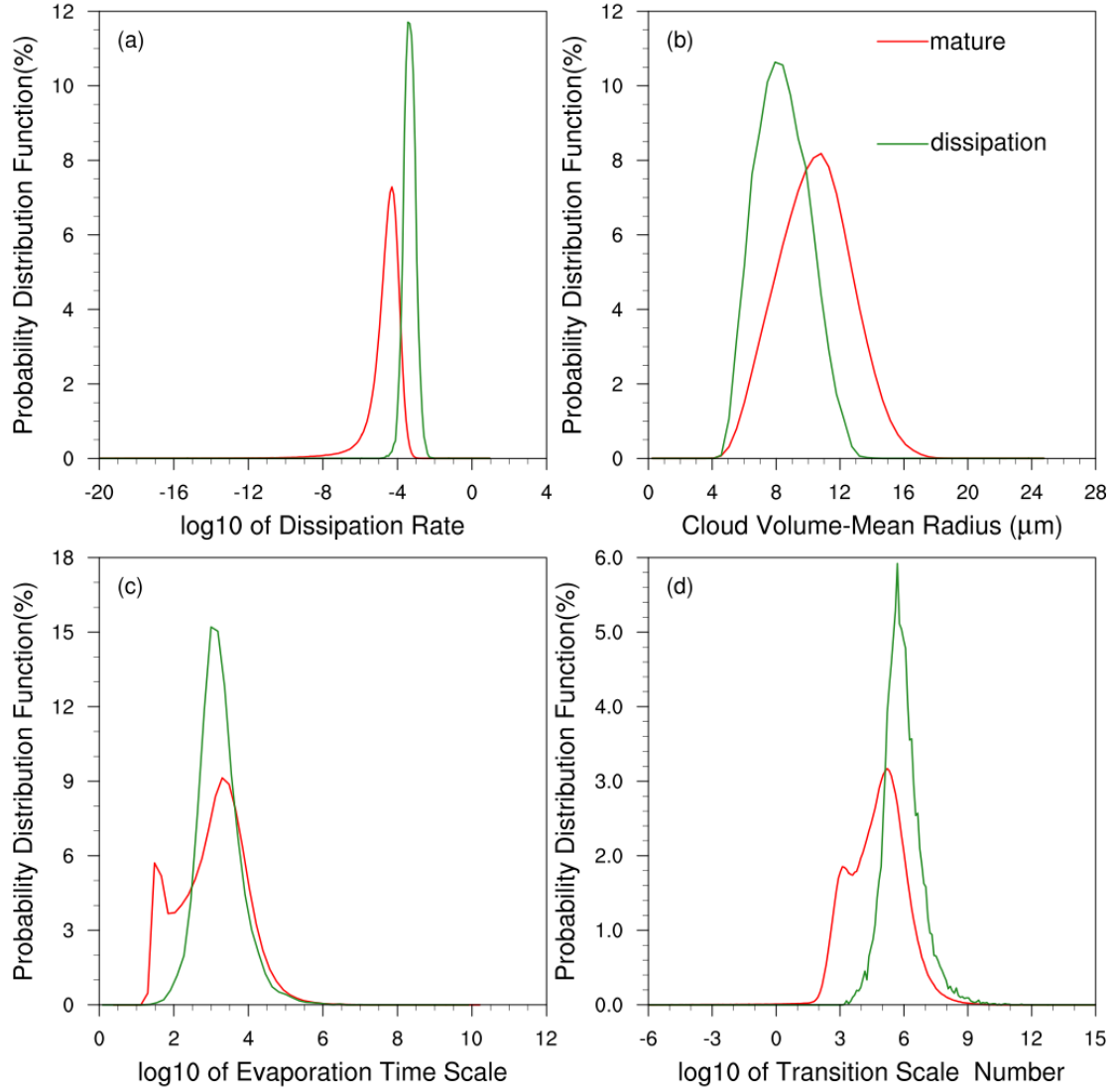
Figure 7. Probability distribution functions (PDFs) of (a) turbulence dissipation rate (ε),
(b) cloud droplet volume-mean radius (r_v), (c) evaporation time scale (τ_{evap}), and (d)
transition scale number (N_L) of cloud grids experiencing the entrainment-mixing
process at the mature stage from 12:00 UTC to 16:00 UTC (the red lines) and the
dissipation stage from 21:00 UTC to 24:00 UTC (the green lines) in *new* for the
stratocumulus case. The experiment is detailed in Table 1.
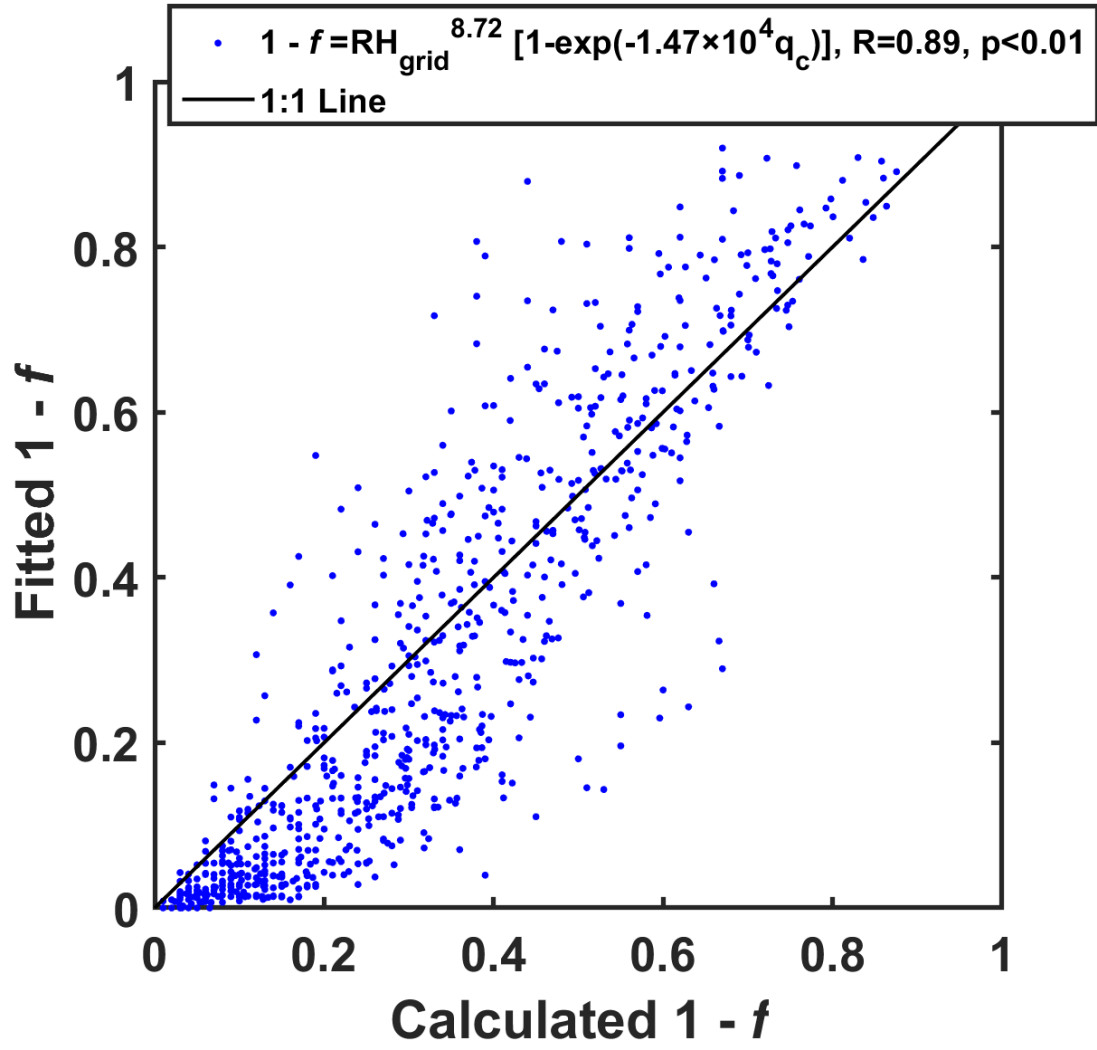
820

821   Figure 8. The fitted $1 - f$ as a function of the calculated $1 - f$. The fitted $1 - f$ is obtained

822   by the fitting functions with grid-mean relative humidity (RH_{grid}) and cloud water

823   mixing ratio (q_c). The black line denotes the 1:1 line.
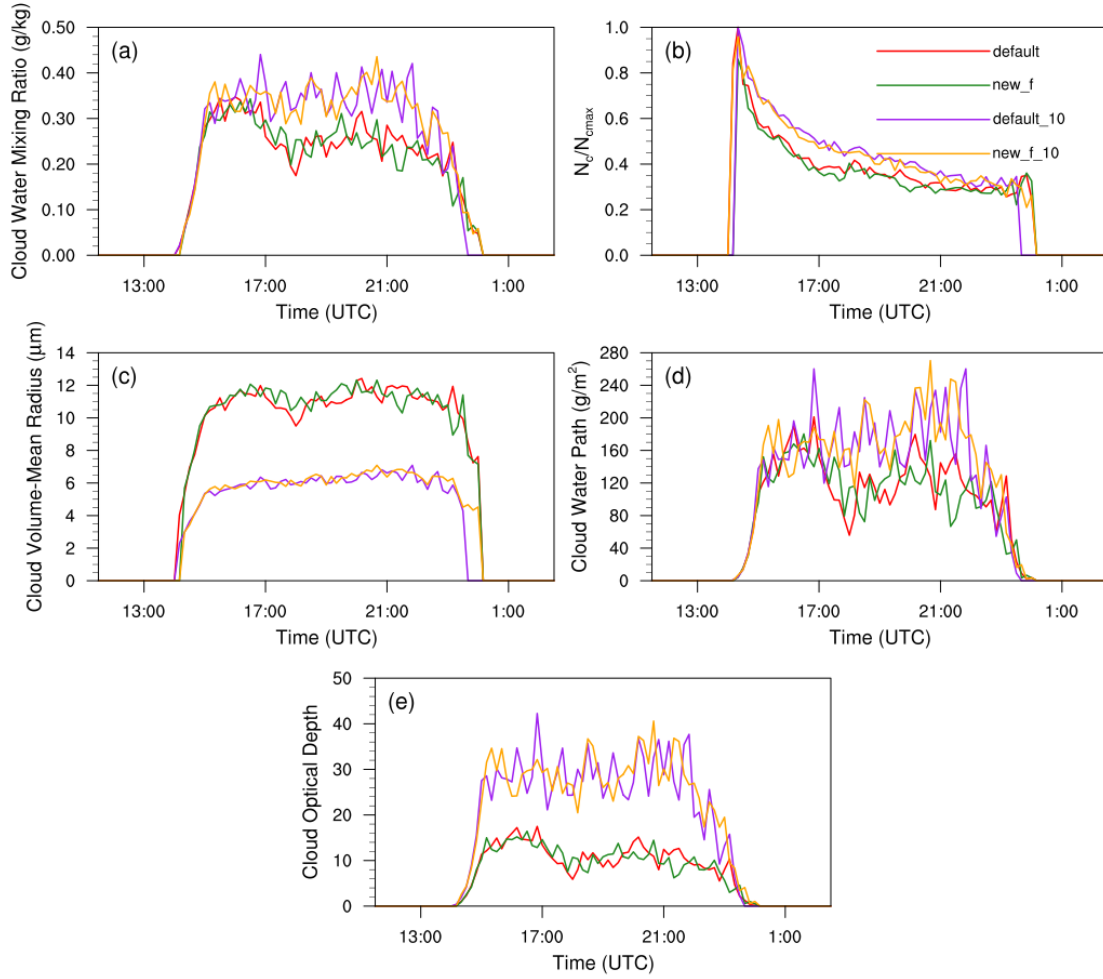
824

825 Figure 9. The temporal evolutions of main cloud microphysical and optical properties

826 in all simulation experiments for the cumulus case, including (a) cloud water mixing

827 ratio (q_c) (g/kg), (b) cloud droplet number concentration (N_c) (/cm^3), (c) cloud droplet

828 volume-mean radius (r_v) (µm), (d) cloud water path (CWP) (g/m^2), and (e) cloud optical

829 depth (τ). In (b), N_c in the experiments *default* and *new_f* are normalized by the

830 maximum cloud droplet concentration (N_{cmax}) from *default*, respectively; N_c in the

831 experiments *default_10* and *new_f_10* are normalized by N_{cmax} from *default_10*,

832 respectively. *new_f* and *new_f_10* are the experiments using entrained air relative

833 humidity.

834
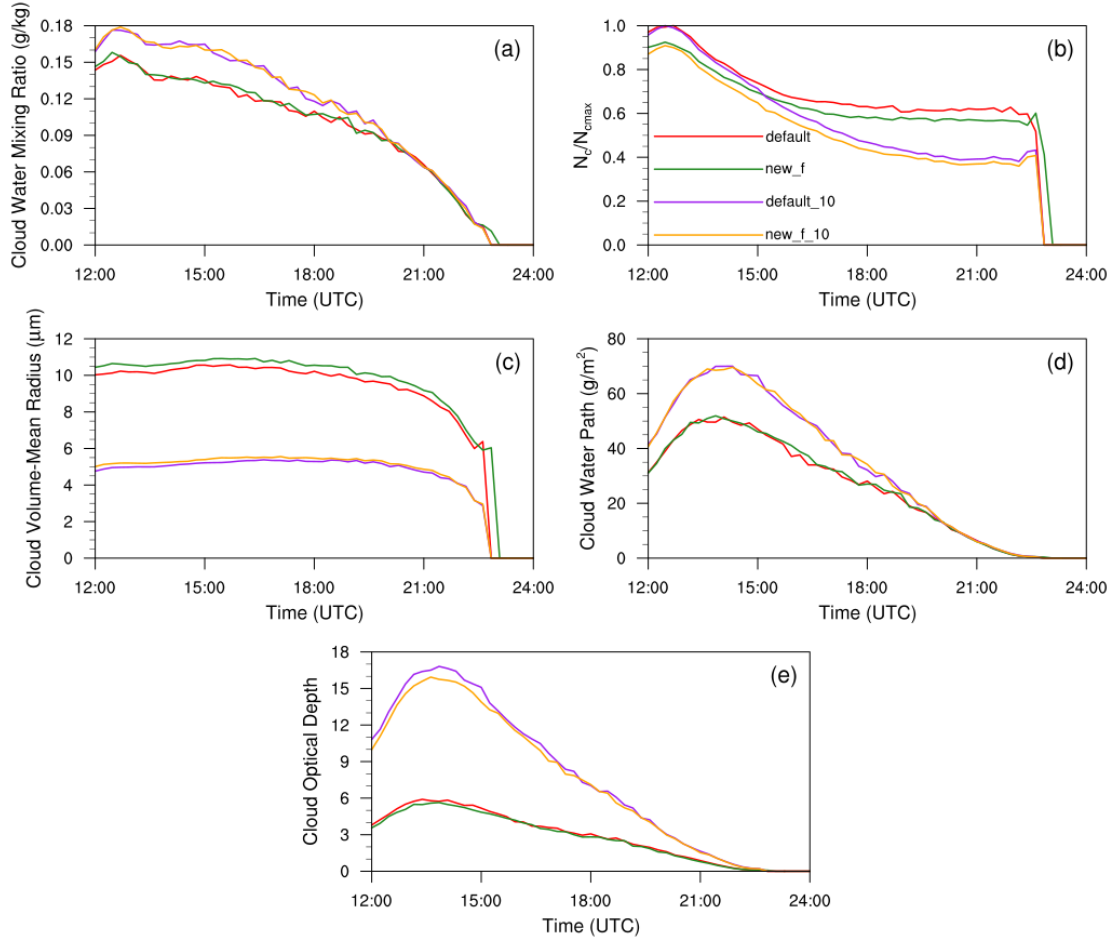
Figure 10. The temporal evolutions of main cloud microphysical and optical properties in all simulation experiments for the stratocumulus case, including (a) cloud water mixing ratio (q_c) (g/kg), (b) cloud droplet number concentration (N_c) (/cm^3), (c) cloud droplet volume-mean radius (r_v) (μm), (d) cloud water path (CWP) (g/m^2), and (e) cloud optical depth (τ). In (b), N_c in the experiments *default* and *new* are normalized by the maximum cloud droplet number concentration (N_{cmax}) from *default*, respectively; N_c in the experiments *default_10* and *new_10* are normalized by N_{cmax} from *default_10*, respectively. *new_f* and *new_f_10* are the experiments using entrained air relative humidity.

844